

# Direct numerical simulation of dense bubbly flows using an improved immersed boundary method

Vahid Tavanashad<sup>a,b</sup>, Shankar Subramaniam<sup>a,b,\*</sup>

<sup>a</sup>*Department of Mechanical Engineering, Iowa State University, Ames, IA 50011, USA*

<sup>b</sup>*Center for Multiphase Flow Research & Education (CoMFRE), Iowa State University, Ames, IA 50011, USA*

---

## Abstract

Fully resolved simulation of flows with bubbles or buoyant particles is a challenging problem due to the fact that bubbles or buoyant particles are lighter than the surrounding fluid and as a result, two phases are strongly coupled together which means using weak coupling methods (explicit coupling schemes) are numerically unstable. Schwarz et al. [Schwarz, S., Kempe, T., & Fröhlich, J. (2015). A temporal discretization scheme to compute the motion of light particles in viscous flows by an immersed boundary method. *J. Comput. Phys.*, 281, 591–613] introduced the virtual force technique to stabilize the immersed boundary method for fully-resolved direct numerical simulation of buoyant particles. They designed a numerical scheme based on this technique to obtain accurate results for the simulation of a single rising sphere with the particle-fluid density ratio of 0.001. In this work, the virtual force stabilization technique is generalized and extended to simulate bubbly flows in contaminated liquid with high volume fractions (up to 40%). Through a detailed analysis, it is shown that the dimensionless numerical model constant  $C_v$  in the virtual force method has a lower limit which depends on density ratio, added mass coefficient and the numerical method. Since the added mass coefficient increases with an increase

---

☆This is a pre-print of an article submitted to *Journal of Computational Physics*.  
©2019. This manuscript version is made available under the CC-BY-NC-ND 4.0 license  
<http://creativecommons.org/licenses/by-nc-nd/4.0/>.

\*Corresponding author

*Email address:* shankar@iastate.edu (Shankar Subramaniam)

in volume fraction, it is concluded that  $C_v$  should also increase with volume fraction. The extended virtual force method is validated for a single bubble and for two in-line rising bubbles by comparing the numerical results with experimental results from the literature. Finally, the drag coefficient is extracted from simulations of bubble swarms at different volume fractions and compared with drag correlations available in the literature.

*Keywords:* contaminated bubble, bubble swarm, buoyant particle, immersed boundary method, fully-resolved direct numerical simulation, drag coefficient

---

## 1. Introduction

Bubbly flows are a type of dispersed multiphase flow where gas bubbles are distributed within a liquid. An important application of bubbly flows is in bubble column reactors where the presence of bubbles enhances heat and mass transfer. Fully-resolved direct numerical simulations (FR-DNS) of bubbly flows are used as a tool for discovering flow physics as well as model development for macro-scale simulations such as Eulerian–Eulerian or Eulerian–Lagrangian approaches [1]. As a result, it is necessary to develop numerical methods that are accurate, convergent, and stable over a wide range of physical parameters: especially gas to liquid density ratio and volume fraction of bubbles.

An important factor that affects the flow physics in bubbly flows is the purity of the surrounding liquid [2–4]. It is shown in many experimental studies [5–9] that the rise velocity of a single bubble is significantly higher in clean systems, like in pure water, in comparison to contaminated systems, like tap water, especially in parameter ranges where the shape of the bubble is spherical or ellipsoidal. Moreover, these studies show that small spherical bubbles in contaminated systems behave like solid spheres. This means that the simulation of bubbles with the no-slip velocity boundary condition at the interface of two phases instead of free-slip is a good approximation for contaminated bubbly flows. Therefore, we use the term *particle* in general for both solid particles and bubbles in this paper.

Over time, different numerical methods have been developed and improved for FR-DNS of bubbly flows in both clean [10–19] and contaminated liquid [20–22]. In tracking methods such as volume-of-fluid [11–13], level-set [14, 15], and front-tracking [18, 21], the boundary condition at the interface is inherently satisfied by the variable density and viscosity and the position of bubbles is updated by tracking the interface. On the other hand, the motion of bubbles is determined from Newton’s equations of motion in immersed boundary [19, 22], lattice Boltzmann [16, 17], or body-fitted [10, 20] methods and the free-slip or no-slip boundary condition is explicitly or implicitly imposed on the interface. In spite of these differences, the original versions of all these methods are numerically unstable if the density ratio is very small unless special care is taken [23–30].

When loose coupling schemes are used in the second group of methods, the interface boundary conditions may not be satisfied accurately since these schemes only involve the solution of the fluid and the particle once per time step. This incompatibility of the kinematic and dynamic quantities at the interface may cause severe stability issues when the particle density  $\rho_p$  is close or smaller than the fluid density  $\rho_f$ . This numerical instability is known as the artificial added-mass effects of the fluid on the particle and is common in fluid–structure interaction problems [31–34]. Although the usage of strong coupling methods (implicit coupling schemes) solve the instability problem at the cost of computational time [35–37], numerous studies have attempted to stabilize explicit coupling schemes to overcome the problem and benefit from the simplicity of explicit methods [38–40].

In the present study, we are going to develop a stabilized explicit coupling scheme for FR-DNS using the immersed boundary method (IBM) that is capable of simulating buoyant rigid particles which are a reasonable approximation to contaminated bubbly flows, as explained. Several studies have shown that the IBM becomes unstable for low-density ratios. [26–30]. For instance, the original work of Uhlmann [26] becomes unstable when the density ratio  $\rho_p/\rho_f$  is smaller than 1.2. In an effort to improve the stability range, Kempe and Fröhlich

[27] succeeded in performing simulations with density ratio as low as 0.4 by numerical evaluation of volume integrals in the equation of particle motion, instead of using the rigid body assumption made by Uhlmann. Yang and Stern [29] utilized the rigid body assumption but used a 4th-order predictor-corrector scheme to solve the equation of motion for particles and achieved stable solution for  $\rho_p/\rho_f > 0.29$ . Our implementation of IBM [41, 42] which is called the particle-resolved uncontaminated-fluid reconcilable immersed boundary method (PUREIBM) directly calculates the hydrodynamic force on each particle from pressure and viscous stress fields, and it is stable for  $\rho_p/\rho_f > 0.07$  (see section 5.1.1). Yang and Stern [43] and Tschisgale et al. [44] have also developed a non-iterative implicit IBM and improved the range of stability for single particle simulations to density ratio 0.1 and 0.001, respectively.

Another promising work in this respect is done by Schwarz et al. [45]. In this work, a virtual force stabilization technique is introduced which allows simulation of a single rising particle with density ratio as low as 0.001. In this technique, the equations are solved using an explicit method and a virtual force is added to the equation of particle motion to stabilize the method. This idea was originally used for a single rising particle and later was used for very dilute systems of contaminated bubble swarms with volume fraction up to 2.14% [22]. The focus of the work by Schwarz et al. [45] is on numerical accuracy. They tried to design a numerical scheme that gives the same accuracy as their original method without the virtual force. The virtual force method has a dimensionless numerical model constant  $C_v$ , which represent the magnitude of the dimensionless virtual force in the particle equation of motion, and Schwarz et al. [45] claimed that this method works for any  $C_v$  greater than zero.

In this paper, we show through detailed analysis that there is a lower positive limit for  $C_v$  which depends on the density ratio, the added mass coefficient, and the numerical method. This condition is important in the case of bubble swarms when compared to a single bubble because the added mass coefficient is affected by the volume fraction and it is important to choose a  $C_v$  value that results in stable solutions for bubbly flows. The ultimate goal of this work is to develop

a method which is accurate, convergent, and stable for simulation of bubbly flows in contaminated liquid for arbitrary density ratio and a range of volume fractions. In this regard, the extended virtual force method is validated for a single bubble and for two in-line rising bubbles by comparing the numerical results with experimental results from the literature. Then, the drag coefficient is extracted from simulations of bubble swarms at different volume fractions and compared with drag correlations available in the literature, as an illustrative example to show the applicability of this method in practice.

Although in this study, we use the virtual force stabilization technique for simulation of buoyant solid spheres as an approximation for small spherical bubbles in contaminated liquid, this technique can be used for any boundary condition (no-slip and free-slip) and for any shape of the particles. Moreover, this technique is not restricted to IBM and could be used in any flow solver in which the motion of bubbles or buoyant particles is determined from Newton's equations of motion.

The rest of the paper is organized as follows: In section 2, the reason behind the instability that occurs in simulations of light particles is explained. In section 3, the virtual force concept is introduced and a detailed explanation is provided as to why and how it works. Then it is generalized and extended for simulating bubble swarms. In section 4, the IBM used in this work is introduced and modifications which are done on the original method to incorporate the virtual force are explained. In section 5, the new method is validated and simulation results for dense bubbly flows are presented. Finally, conclusions are drawn in section 6.

## **2. Numerical instability in simulations of strongly coupled particle-fluid flows**

Although the final goal of this study is to perform fully resolved simulation, for simplicity, the instability problem that occurs in low-density-ratio simulations is first explained through point particle equations in this section. The

extension to fully resolved simulation is discussed in section 3.3.

In the point particle approach, the interaction between particles and the surrounding flow is modeled. In this case, the equation of motion for particles is described using the Basset-Boussinesq-Oseen (BBO) equation,

$$m_p \frac{d\mathbf{u}_p}{dt} = \mathbf{F}_D + \mathbf{F}_L + \mathbf{F}_{AM} + \mathbf{F}_{BH} + \mathbf{F}_B, \quad (1)$$

where  $\mathbf{u}_p$  is the particle velocity,  $m_p$  is the particle mass,  $\mathbf{F}_D$  denotes the drag force,  $\mathbf{F}_L$  the lift force,  $\mathbf{F}_B$  the body forces,  $\mathbf{F}_{AM}$  the added mass force and  $\mathbf{F}_{BH}$  the Basset history force. All or some of these forces need to be modeled and included in the simulations depending on the problem.

In this equation, the added mass force is defined as:

$$\mathbf{F}_{AM} = m_{am} \left( \frac{D\mathbf{u}}{Dt} - \frac{d\mathbf{u}_p}{dt} \right), \quad (2)$$

where  $\mathbf{u}$  is the fluid velocity at the particle location and  $m_{am}$  is the added mass which is usually defined by a dimensionless coefficient  $C_{am}$  as  $m_{am} = C_{am}\rho_f V_p$ , where  $\rho_f$  is density of fluid and  $V_p$  is volume of particle. Added mass represents the inertia added to a particle as it accelerates (or decelerates) and moves (or deflects) a portion of its surrounding fluid.

Hu et al. [35] have shown that Eq. (1) is unstable when it is solved with an explicit time integration method and the added mass exceeds the particle mass. They assume that at early stages of motion only body forces and added mass force are important. Furthermore, they assume that at early stages the fluid acceleration is much smaller than the particle acceleration. Under these assumptions, Eq. (1) simplifies to:

$$m_p \frac{d\mathbf{u}_p}{dt} = \mathbf{F}_B - m_{am} \frac{d\mathbf{u}_p}{dt}. \quad (3)$$

Note that  $\mathbf{F}_B = (\rho_p - \rho_f) V_p \mathbf{g}$  is a constant driving force and  $\rho_p$  is the particle density. Starting from an initial condition and solving this equation for the next time step, it can be shown that acceleration at time step  $n$  is related to

the initial acceleration through the following equation [35],

$$\frac{d\mathbf{u}_p}{dt}(t_n) = \frac{1 - \left(-\frac{m_{am}}{m_p}\right)^n}{m_p + m_{am}} \mathbf{F}_B - \left(-\frac{m_{am}}{m_p}\right)^n \frac{d\mathbf{u}_p}{dt}(t_0). \quad (4)$$

Equation (4) shows that the particle velocity oscillates with increasingly large amplitude when the added mass is larger than the mass of particle, i.e.,  $m_{am} > m_p$ . Therefore, the stability condition for Eq. (4) is:

$$m_p > m_{am} \Rightarrow \rho_p / \rho_f > C_{am}, \quad (5)$$

which means density ratio should be greater than the added mass coefficient to have stable solution.

The solution of Eq. (1) for very low-density ratios is straightforwardly stabilized by moving the term with particle acceleration in the added mass force to the left-hand side (LHS) of the equation which yields stable time integration. Although it is easy to stabilize this equation, the final goal in this paper is to perform fully resolved simulation of particle flows in which the force on each particle is directly calculated from the velocity and pressure fields (see section 3.3) and it is not possible to separate forces easily as in this case where the forces are modeled. Therefore, a different strategy is needed which is introduced in the next section.

### 3. Concept of virtual force stabilization technique

#### 3.1. Background and accuracy discussion

Schwarz et al. [45] introduced the virtual force technique to stabilize the equation of motion for particles in the case of low density ratio. They defined a *generic* test case for the sedimentation or rise of a sphere in quiescent, unbounded fluid in the Stokes flow regime and wrote the translational particle momentum equation as:

$$m_p \frac{du_p}{dt} = F_{D,Stokes} + F_B, \quad (6)$$

where  $F_{D,Stokes} = -3\pi d_p \mu_f u_p$  is the Stokes' drag force,  $d_p$  is the particle diameter, and  $\mu_f$  is the fluid dynamic viscosity.

Then they defined the virtual force as:

$$\mathbf{F}_v = C_v \rho_f V_p \frac{d\mathbf{u}_p}{dt}, \quad (7)$$

with  $C_v$  an appropriately chosen coefficient. Although the virtual force is defined similar to the added mass force, it is a purely mathematical term designed to stabilize the temporal integration and does not have any physical meaning. Adding this force to both sides of Eq. (6) gives:

$$(m_p + C_v \rho_f V_p) \frac{du_p}{dt} = F_{D,Stokes} + F_B + F_v. \quad (8)$$

Schwarz et al. [45] explained their reasoning for doing this by saying that the solution of Eq. (6) “becomes problematic when  $\rho_p/\rho_f \rightarrow 0$  and thus  $m_p \rightarrow 0$ , as then the LHS of Eq. (6) becomes singular.” The virtual force removes “the singularity on the LHS when  $\rho_p \rightarrow 0$  for  $C_v > 0$ ” since now the term  $(\rho_p + C_v \rho_f)V_p$  is on the LHS of Eq. (8) which does not go to zero for small  $\rho_p$  and  $C_v > 0$ . While it is true that the solution of Eq. (6) with an explicit time integration method becomes unstable with decreasing  $m_p$ , this instability could be overcome by decreasing the time step since it is a conditionally unstable situation. On the other hand, the instability introduced in section 2 is an unconditionally unstable situation in which decreasing time step does not help. This means the explanation provided by Schwarz et al. [45] is inaccurate.

As discussed in section 2, the presence of the added mass force is the underlying reason for the instability problem at low-density ratios and not the singularity of LHS of Eq. (6) when  $m_p$  becomes small. In other words, Eq. (6) is conditionally stable even for very small  $m_p$  since the added mass force is not considered in this *generic* test case. In spite of this, the virtual force technique is useful and also solves the unconditionally unstable situation. However, there is a positive lower limit for  $C_v$  that prevents the instability whereas Schwarz et al. [45] claimed it is only required  $C_v$  to be greater than zero. This point is

the topic of the next subsection where it is shown how the exact condition on  $C_v$  for achieving a stable solution obtained by using a test case that includes the added mass force.

Before finishing this section, it is important to mention that Schwarz et al. [45] used their generic test case to design a numerical technique that gives the same accuracy as their original method without virtual force. In this regard, their test case is useful and valid but it cannot be used for studying the stability condition.

### 3.2. Stability discussion

In this section, we show that there is a lower limit for  $C_v$  to stabilize the problem and then a new test case is introduced that includes the added mass force. Starting with Eq. (3) and adding the virtual force to this equation results in:

$$m_p \frac{d\mathbf{u}_p}{dt} + \mathbf{F}_v = \mathbf{F}_B - m_{am} \frac{d\mathbf{u}_p}{dt} + \mathbf{F}_v. \quad (9)$$

By defining  $m_p^{eq} = m_p + C_v \rho_f V_p$  and  $m_{am}^{eq} = m_{am} - C_v \rho_f V_p$ , this equation is re-written as:

$$m_p^{eq} \frac{d\mathbf{u}_p}{dt} = \mathbf{F}_B - m_{am}^{eq} \frac{d\mathbf{u}_p}{dt}. \quad (10)$$

It is clear that Eqs. (3) and (10) are similar and it is concluded that the latter equation is only stable if  $m_p^{eq} > m_{am}^{eq}$  which simplifies to:

$$\frac{m_p^{eq}}{m_{am}^{eq}} > 1 \Rightarrow \frac{\rho_p + C_v \rho_f}{(C_{am} - C_v) \rho_f} > 1 \Rightarrow C_v > \frac{C_{am}}{2} - \frac{\rho_p}{2\rho_f}. \quad (11)$$

This result shows that there is a lower limit for  $C_v$  which depends on the added mass coefficient and the density ratio whereas Schwarz et al. [45] claimed it is only required  $C_v$  to be greater than zero.

We modify the generic test case of Schwarz et al. [45] (Eq. (6)) by adding the added mass force because this is the real test of the instability identified by

[35]. This yields,

$$m_p \frac{du_p}{dt} = F_{D,Stokes} + F_B + F_{AM}, \quad (12)$$

where  $F_{AM} = -C_{am}\rho_f V_p \frac{du_p}{dt}$  is the added mass force. The added mass coefficient is obtained from potential flow theory to be  $C_{am} = 0.5$  for a sphere, and this value is widely used in the literature even for viscous flows.

To solve Eq. (12), one needs to numerically calculate  $du_p/dt$  on the right-hand side (RHS) and then numerically integrate the equation to calculate  $u_p$  in time. Considering the stability condition in Eq. (5), it is expected that the solution of Eq. (12) becomes unstable for  $\rho_p/\rho_f < 0.5$ . To test this condition, we used different numerical methods where the details of each method are presented in Appendix A.

Our experience for solving Eq. (12) shows that some numerical methods are unstable even when Hu's criterion (Eq. (5)) [35] is satisfied whereas some are stable even when Hu's criterion is not satisfied. Table (1) summarizes the behavior of different numerical methods. Each method has a minimum  $\rho_p/\rho_f$  below which simulations are unstable (without virtual force), which is reported in the  $(\rho_p/\rho_f)_{min}$  column. To explain this discrepancy, we note that equation (12) includes the drag force and is not exactly the same equation which was used in Hu's analysis. In addition, Hu et al. [35] calculated the acceleration of the particle at each time step based on the acceleration in the previous time step which is not the case in predictor-corrector numerical schemes. These differences could be the reason why different numerical methods have different limits for the minimum density ratio at which stable solutions are obtained without virtual force stabilization.

To overcome the instability problem in Eq. (12) for low-density ratios, we add the virtual force to both sides of this equation and simplify it to:

$$(\rho_p + C_v \rho_f) V_p \frac{du_p}{dt} = F_{D,Stokes} + F_B - (C_{am} - C_v) \rho_f V_p \frac{du_p}{dt}. \quad (13)$$

As discussed, Hu's criterion is not exactly valid for all numerical methods.

Therefore, Eq. (11), which is derived based on Hu's criterion and gives the minimum  $C_v$  to be used in virtual force stabilization, is also not valid. In order to fix this problem, we extend Hu's stability criterion ( $\rho_p/\rho_f > C_{am}$ ) and consider the role of the numerical method in our analysis by assuming that the lower limit for the density ratio is a factor  $\lambda$  times  $C_{am}$ , where  $\lambda$  depends on the numerical method used. This results in a modified stability criterion (compare with Eq. (5)):

$$\frac{\rho_p}{\rho_f} > \lambda C_{am} \Rightarrow \frac{\rho_p}{\rho_f C_{am}} > \lambda, \quad (14)$$

where  $\lambda$  is a constant and is determined specifically for each numerical method. By extending this relation to equivalent masses introduced in Eq. (10), we have (compare with Eq. (11)):

$$\frac{\rho_p + C_v \rho_f}{(C_{am} - C_v) \rho_f} > \lambda \Rightarrow C_v > \frac{\lambda C_{am}}{\lambda + 1} - \frac{\rho_p}{(\lambda + 1) \rho_f}, \quad (15)$$

which gives a new criterion on the minimum value of  $C_v$  for each  $\lambda$  which depends on numerical method.

To verify this new criterion, we tested different numerical methods and calculated the minimum  $C_v$  that stabilizes the method for  $\rho_p/\rho_f = 0.001$  using the condition derived in Eq. (15). First, using the  $(\rho_p/\rho_f)_{min}$  for each method and Eq. (14),  $\lambda$  is calculated for  $C_{am} = 0.5$  (a single sphere). After that, the minimum  $C_v$  that stabilizes the method for  $\rho_p/\rho_f = 0.001$  is calculated using Eq. (15) and reported in the  $C_v^{min}$  column of Table (1) which also stabilizes the method in practice.

Note that in solving Eq. (13), the special case of  $C_v = C_{am}$  is similar to moving the added mass force to the LHS of Eq. (12), which as we discussed earlier is a possible solution in the case of point particles but cannot be extended to fully resolved simulation.

Table 1: Stability characteristics of different numerical methods for solving the new test problem included added mass force and drag (Eq. (12)). For each numerical method, there exists a minimum  $\rho_p/\rho_f$  below which simulations are unstable without virtual force stabilization, which is reported in the  $(\rho_p/\rho_f)_{min}$  column. Using this value and Eq. (14),  $\lambda$  is calculated for  $C_{am} = 0.5$ . The minimum  $C_v$  that stabilizes each method for  $\rho_p/\rho_f = 0.001$  is calculated using Eq. (15) and reported in the  $C_v^{min}$  column.

| Solution Method | Calculation of $(\rho_p/\rho_f)_{min}$ | $\lambda$ | $C_v^{min}$ |
|-----------------|--|-----------|-------------|
| Euler           | 1st order BW                           | 0.5       | 0.25        |
| AB2             | 2nd order BW                           | 2.1       | 0.40        |
| RK3             | 3rd order BW                           | 1.7       | 0.38        |
| Euler           | AB-predictor                           | 0.38      | 0.21        |
| AB2             | AB-predictor                           | 0.57      | 0.26        |
| RK3             | AB-predictor                           | 0.38      | 0.21        |

In summary, the value of  $C_v^{min}$  for stable simulation depends on the density ratio, the added mass coefficient, and the numerical method through  $\lambda$ . It is known that the geometry of the individual particle and the presence of other particles or bounding walls can affect the added mass coefficient [46], so it is expected that the physics of the problem affects the stability condition on  $C_v$  through the added mass coefficient which is confirmed in section 5.3 where we simulate bubble swarms. It should also be noted that while there is not an upper limit for  $C_v$ , a very large  $C_v$  (say one order of magnitude larger than  $C_v^{min}$ ) leads to a conditionally unstable solution which can be overcome by decreasing the time step. Moreover, Schwarz et al. [45] have shown that to keep the same order of convergence as the original method without virtual force it is necessary to use a predictor-corrector scheme to calculate  $du_p/dt$  on the RHS of Eq. (13). Therefore, using a predictor-corrector scheme with  $C_v > C_v^{min}$  will result in a *stable and accurate* solution to the model equation with the added mass force (ref. Eq. (13)).

Up to this point, the discussion was about stabilizing the equation of particle

motion in point particle simulations. In the next section, we discuss the use of virtual force stabilization in FR-DNS.

### 3.3. Fully resolved simulations

In FR-DNS, particles are fully resolved by the grid and the flow field on the surface of each particle is captured by solving the Navier-Stokes equations. The hydrodynamic force on each particle is calculated by integrating the pressure and viscous stress fields over the particle surface, and the resulting equation of motion for each particle is,

$$m_p \frac{d\mathbf{u}_p}{dt} = \rho_f \oint_{\Gamma_p} \boldsymbol{\tau} \cdot \mathbf{n} ds + (\rho_p - \rho_f) V_p \mathbf{g}, \quad (16)$$

where  $\boldsymbol{\tau} = -\mathbf{I}p/\rho_f + \nu(\nabla\mathbf{u} + \nabla\mathbf{u}^T)$  is the hydrodynamic stress tensor with  $\mathbf{I}$  the identity matrix,  $p$  is the pressure with the hydrostatic part being subtracted,  $\mathbf{n}$  is the normal vector at the surface of particle, and  $\mathbf{g}$  is the acceleration due to the gravity.

In FR-DNS, the surface integrals in Eq. (16) are evaluated directly from the flow field yielding all forces acting on the particle. As mentioned in the introduction, the solution of this equation also becomes problematic for low-density ratios as reported in the literature [26–30]. Similarly, our code, PUREIBM, also becomes unstable for low-density ratios,  $\rho_p/\rho_f < 0.07$ . Therefore, it is important to apply the virtual force technique in PUREIBM to stabilize the fully resolved simulations for low-density ratios which is the topic of section 4.

#### 3.3.1. Generalization of virtual force concept

We can understand virtual force stabilization as a technique to add some *implicitness* to an explicit time marching scheme by recognizing that the presence of forces on RHS of Eqs. (3) or (12) that are proportional to  $\frac{d\mathbf{u}_p}{dt}$  can destabilize the scheme unless the equation is integrated with some degree of implicitness by absorbing them through modified coefficients of  $\frac{d\mathbf{u}_p}{dt}$  on the LHS. In FR-DNS, only the total hydrodynamic force is known and it is different for each particle. Therefore, an alternative approach is introduced here which is

the generalization of the virtual force by using a  $C_v$  that can be different for each particle. In this version,  $C_v$  is defined as:

$$C_v = \frac{m_v}{\rho_f V_p}, \quad (17)$$

where  $m_v$  is the virtual mass.

The basic idea here is that we subtract the drag force  $\mathbf{F}_d$  from the total hydrodynamic force  $\mathbf{F}_h = \rho_f \oint_{\Gamma_p} \boldsymbol{\tau} \cdot \mathbf{n} ds$  acting on a particle and decompose the remainder into two contributions: its projection along with the particle acceleration and orthogonal to the particle acceleration. The component aligned with the particle acceleration plays the role of an *effective* added mass force and can be dealt with as in Eq. (13). Therefore, to calculate  $m_v$  in Eq. (17), the hydrodynamic force on each particle is decomposed as  $\mathbf{F}_h = \mathbf{F}^n + \mathbf{F}_d + \mathbf{F}_{am}^*$  where  $\mathbf{F}^n$  is the normal component of the force to the particle acceleration,  $\mathbf{F}_d$  is the drag force aligned with the slip velocity between particle and fluid, and  $\mathbf{F}_{am}^* = m_v \frac{d\mathbf{u}_p}{dt}$  is the component aligned with the acceleration which is the effective added mass force. The dot product of hydrodynamic force with particle acceleration gives:

$$(\mathbf{F}_h = \mathbf{F}^n + \mathbf{F}_d + \mathbf{F}_{am}^*) \cdot \frac{d\mathbf{u}_p}{dt} \Rightarrow m_v = \frac{\mathbf{F}_h \cdot \mathbf{a}_p - \mathbf{F}_d \cdot \mathbf{a}_p}{\mathbf{a}_p \cdot \mathbf{a}_p}, \quad (18)$$

where  $\mathbf{a}_p$  is the particle acceleration. Using this relation and a drag law for  $\mathbf{F}_d$ , one can calculate  $m_v$  as:

$$(m_p + m_v) \frac{d\mathbf{u}_p}{dt} = \rho_f \oint_{\Gamma_p} \boldsymbol{\tau} \cdot \mathbf{n} ds + (\rho_p - \rho_f) V_p \mathbf{g} + m_v \frac{d\mathbf{u}_p}{dt}, \quad (19)$$

In this approach,  $m_v$  (and  $C_v$ ) will change from one particle to another, however, in practice, the value of  $m_v$  and consequently  $C_v$  sometimes becomes negative. This is due to the fact that the mean drag is used in Eq. (18) while it is known that the drag force on each particle could be significantly different from mean drag force [47–49] Some particles will experience larger drag force which results in high  $C_v$  and some will experience lower drag force which results

in negative  $C_v$ . As discussed in section 3, there exist a positive minimum value for  $C_v$ , so negative values are not acceptable.

To solve this problem with the negative values of  $C_v$ , one idea is to limit the  $C_v$  from Eq. (18) with minimum  $C_v$  of a single particle. As shown in Appendix B, even, in this case, there exists large oscillation in the mean drag force. Therefore, in the rest of the paper, the approach with constant  $C_v$  is followed.

#### 4. Numerical method for FR-DNS

The fully resolved simulation approach used in this work is based on the direct forcing immersed boundary method of Mohd-Yusof [50] which is further developed in [41, 42], and is called the particle-resolved uncontaminated-fluid reconcilable immersed boundary method (PUREIBM). The PUREIBM methodology is explained in detail in other works [42, 47, 51] and has been extensively validated in different cases [41, 47, 52]. Here, the main features of this method are presented.

The governing equations of the fluid phase that are solved in PUREIBM are the continuity equation:

$$\nabla \cdot \mathbf{u} = 0, \quad (20)$$

and the Navier-Stokes equations:

$$\frac{\partial \mathbf{u}}{\partial t} + \mathbf{S} = -\frac{1}{\rho_f} \nabla p + \nu_f \nabla^2 \mathbf{u} + \mathbf{f}_{\text{IBM}}, \quad (21)$$

which are solved on a uniform Cartesian grid points with the Crank-Nicolson scheme for the viscous terms and an Adams-Bashforth scheme for the convective terms. In Eqs. (20) and (21),  $\mathbf{u}$  is the instantaneous velocity field,  $\mathbf{S} = \nabla \cdot (\mathbf{u}\mathbf{u})$  is the convective term,  $\nabla p$  is the pressure gradient, and  $\nu_f$  is the kinematic viscosity. The boundary conditions on the fluid velocity at the particle interface (no-slip and no-penetration) are imposed via the immersed boundary force term,  $\mathbf{f}_{\text{IBM}}$ .

The motion of each particle in PUREIBM is evolved by updating its position  $\mathbf{X}$ , and translational velocity  $\mathbf{V}$  according to Newton's second law as:

$$\frac{d\mathbf{X}}{dt} = \mathbf{V}, \quad (22)$$

$$m_p \frac{d\mathbf{V}}{dt} = \mathbf{F}_B + \mathbf{F}_h + \sum_{\substack{j=1 \\ j \neq i}}^{N_p} \mathbf{F}_c^{(ij)}, \quad (23)$$

where  $\mathbf{F}_B$  is the body forces,  $\mathbf{F}_h$  is the hydrodynamic force (the integral of pressure and shear stress tensor at the particle surface) and  $\mathbf{F}_c^{(ij)}$  is the collisional force between the  $i^{\text{th}}$  particle and  $j^{\text{th}}$  particle. A soft-sphere collision [53] is used to model the particle-particle interactions. Particles are allowed to overlap during a collision, and the contact mechanics between the overlapping particles is modeled by a spring in the normal direction (elastic collisions). The spring causes the colliding particles to rebound. The particles considered in this study are assumed to be frictionless. This implies that the tangential component of the contact force is zero.

Rotation of each particle in PUREIBM is evolved by updating its rotational velocity,  $\mathbf{\Omega}$ , according to:

$$I_p \frac{d\mathbf{\Omega}}{dt} = \mathbf{T}_h + \sum_{\substack{j=1 \\ j \neq i}}^{N_p} \mathbf{T}_c^{(ij)}, \quad (24)$$

where  $I_p = 1/10\rho_p V_p d_p^2$  is the moment of inertia of particles,  $\mathbf{T}_h$  is the hydrodynamic torque and  $\mathbf{T}_c$  is the collisional torque which is zero for frictionless particles.

In the next sections 4.1 and 4.2, the modifications to the original PUREIBM to extend its capability to simulate buoyant particles are explained.

#### 4.1. Addition of virtual force and torque to PUREIBM

Since Eq. (23) is solved explicitly for the particle acceleration in PUREIBM, some numerical instabilities arise in the code when the density ratio is small.

As discussed in the previous section, the virtual force (Eq. (7)) should be added to both sides of Eq. (23) to stabilize the PUREIBM for low-density ratio simulations,

$$(m_p + C_v \rho_f V_p) \frac{d\mathbf{V}}{dt} = \mathbf{F}_B + \mathbf{F}_h + \sum_{\substack{j=1 \\ j \neq i}}^{N_p} \mathbf{F}_c^{(ij)} + \mathbf{F}_v. \quad (25)$$

Similar to the concept of virtual force, we can define a virtual torque  $\mathbf{T}_v = 1/10 C_v^T \rho_f V_p d_p^2 \frac{d\boldsymbol{\Omega}}{dt}$  and add it to both sides of Eq. (24) to stabilize this equation,

$$\left( I_p + \frac{1}{10} C_v^T \rho_f V_p d_p^2 \right) \frac{d\boldsymbol{\Omega}}{dt} = \mathbf{T}_h + \sum_{\substack{j=1 \\ j \neq i}}^{N_p} \mathbf{T}_c^{(ij)} + \mathbf{T}_v. \quad (26)$$

In the definition of virtual torque,  $C_v^T$  is the virtual torque coefficient and it is considered to be equal to  $C_v$  in this paper.

The Adams-Bashforth predictor-corrector scheme is used to solve Eqs. (25) and (26) which is necessary for having the same order of convergence as the original PUREIBM without virtual force as discussed in [45]. In addition, we follow the same initialization approach used in [45]. The overall order of accuracy and convergence properties of the modified method and the temporal and spatial discretization errors are not changed by adding the virtual force, as mentioned in [45], so a discussion on these topics is not repeated here.

#### 4.2. Lubrication force

In numerical methods based on structured grids such as IBM, the flow field is not accurately resolved when the distance between the surface of particles becomes less than the grid spacing. Therefore, the lubrication force is not completely resolved. To resolve the lubrication force it is necessary to use a fine grid which results in very small time steps for the explicit scheme used here. However, it has been argued in the literature that the details of the lubrication and collision model are only important when the trajectory of an individual particle is investigated, while average statistics of large systems are not affected by these details [54, 55].

In this work, the lubrication force is modeled as [56, 57]:

$$\mathbf{F}_{lub}^{ij} = \begin{cases} 0 & h < \epsilon_{col} \\ -6\pi\mu\frac{d_p^2}{16}\left(\frac{1}{h} - \frac{1}{\epsilon_{lub}}\right)\mathbf{U}_{ij} \cdot \mathbf{n}_{ij} & \epsilon_{col} < h < \epsilon_{lub} \\ 0 & h > \epsilon_{lub} \end{cases}, \quad (27)$$

where  $\mathbf{F}_{lub}^{ij}$  is the lubrication force,  $\mathbf{U}_{ij}$  is relative velocity between particle  $i$  and  $j$ ,  $\mathbf{n}_{ij}$  is unit vector pointing out from the center of particle  $i$  to the center of particle  $j$ ,  $h = |\mathbf{x}_i - \mathbf{x}_j| - d_p$  is the surface-to-surface distance between particles  $i$  and  $j$ ,  $\epsilon_{lub}$  is the cutoff distance beyond which the lubrication force is negligible and  $\epsilon_{col}$  has a nonzero positive value to prevent the singularity in the lubrication force as  $h \rightarrow 0$ . Even with inclusion of the lubrication force, some particles may collide with each other. In this case, we use the same collision model already introduced, but with a small change that the collision starts when  $h < \epsilon_{col}$ , which prevents the lubrication force to become singular. The parameters of lubrication force used in this study are  $\epsilon_{lub}/d_p = 0.5$  and  $\epsilon_{col}/d_p = 0.0003$ , as suggested in the literature [54, 56, 57].

## 5. Results and discussion

In this section, the simulation of a single buoyant particle is presented first, with the goal of the validation. Then, the rise of two in-line buoyant particles is presented and compared with experimental results. Finally, simulations of dense bubbly flows at different volume fraction are presented.

### 5.1. Rise of a single buoyant particle

For the purpose of validation, two different comparisons are done with other numerical and experimental works in the literature. In the first case, the temporal evolution of particle velocity is studied and results are compared with other numerical works. Then, the drag force on a single buoyant particle is compared with the drag on a spherical bubble in contaminated liquid from an experiment.

### 5.1.1. Temporal evolution

The goal of this subsection is to show that the implementation of the virtual force in PUREIBM is done correctly and to validate the numerical simulation. For this purpose, the motion of a single sphere ascending in a quiescent, viscous fluid under the action of gravity is simulated. The input dimensionless parameters are Archimedes number  $Ar$  and density ratio  $\rho_p/\rho_f$ . The Archimedes number is defined as:

$$Ar = \frac{|\rho_p/\rho_f - 1|gd_p^3}{\nu_f^2}. \quad (28)$$

The simulation is performed in a cuboidal domain with periodic boundary conditions in all directions. The length of the domain in the direction of gravity is  $L_x = 12.8d_p$  which is twice the length of the domain in other directions. The particle and fluid are initially at rest and evolve under the action of gravity. A mean pressure gradient is imposed on the system to oppose the effect of gravity and keep the mean fluid velocity zero and then the particle starts to move due to the gravity. Although a condition for  $C_v^{min}$  was derived in Eq. (15) for the case of point particle simulations, there are more parameters that affect the  $C_v^{min}$  in resolved simulations like the grid resolution. For example, the lowest density ratio that is possible to simulate in PUREIBM (without using virtual force stabilization) is  $\rho_p/\rho_f = 0.09$  with grid resolution per particle diameter  $D_m = 20$  and  $\rho_p/\rho_f = 0.07$  with  $D_m = 30$ . The  $C_v^{min}$  for these two cases are 0.15 and 0.11, respectively. In our simulations,  $C_v = 0.15$  is used for the case of a single particle.

Figure 1 shows the region of stability for the simulation of a single rising particle with  $Ar = 1000$  and  $D_m = 20$ . Simulations are unconditionally unstable for  $C_v$  less than  $C_v^{min}$  independent of the grid resolution and time step. This figure also shows that the simulations are stable for  $C_v > C_v^{min}$ , however, to get accurate results it is necessary to limit the time step. In the single bubble simulation under gravity, the velocity at the beginning is very small and using a constant CFL  $CFL = u_{max} \frac{\Delta t}{\Delta x}$  will result in a large time step. Therefore a

constant time step is used in PUREIBM with a condition on the maximum CFL number. If the CFL number becomes larger than the maximum CFL number, then the time step is decreased. For the case shown in Fig. 1, the CFL number does not become larger than the maximum CFL number, and hence the time step remains constant during the simulation.

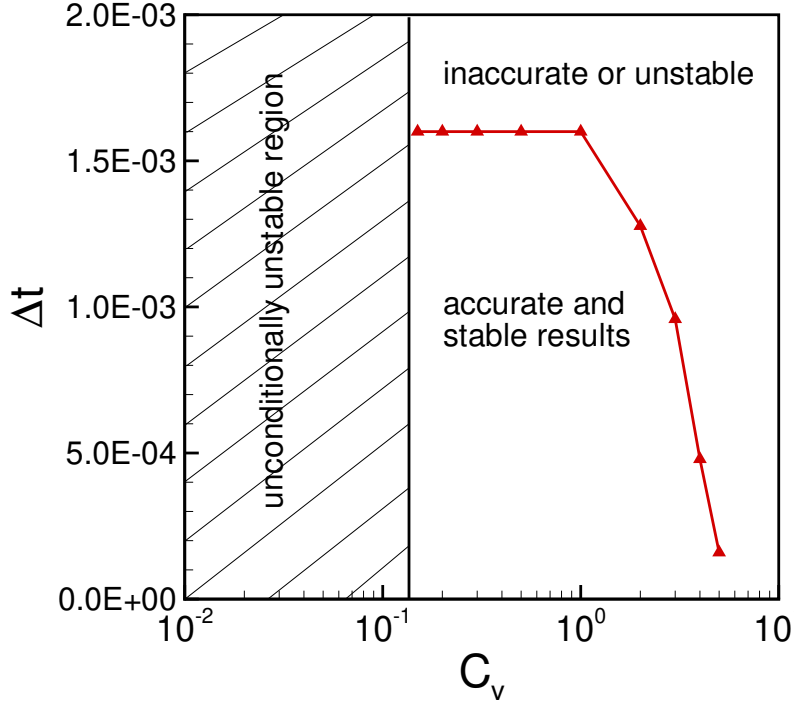


Figure 1: Stability region for the simulation of a single rising particle for  $D_m = 20$ . Simulations are unconditionally unstable for  $C_v$  less than  $C_v^{min} = 0.15$  independent of the grid resolution and time step. The simulations are stable for  $C_v > C_v^{min}$ , however, to get accurate results it is necessary to limit the time step.

To validate these results, they are compared with the numerical simulation using IBM developed by Schwarz et al. [45] and an implicit, highly-resolved spectral body-fitted method developed in Dušek's group [58, 59]. The results from Dušek's group were received by Schwarz et al. [45] in private communication and are published in their work.

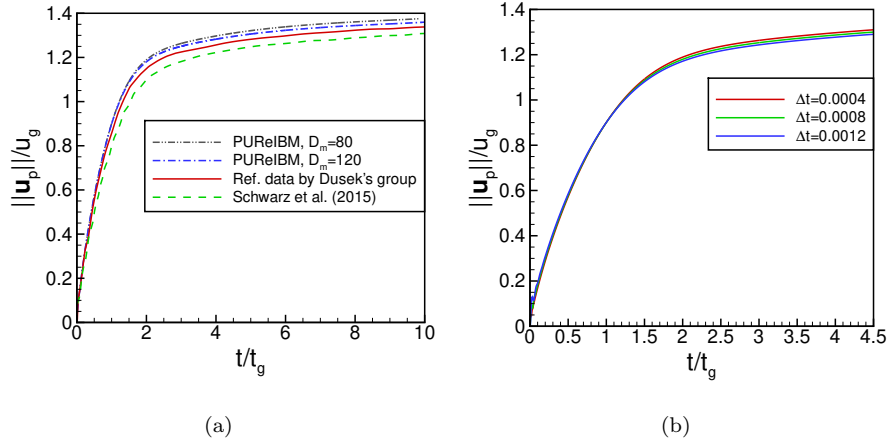


Figure 2: Temporal evolution of a single rising particle for  $Ar = 28900$  and  $\rho_p/\rho_f = 0.001$  (a) Results of PUREIBM with two grid resolutions compared to the reference body-fitted simulation of Dušek's group [58, 59] and the IBM simulation of Schwarz et al. [45]. (b) Convergence of the velocity with decreasing time step for  $D_m = 80$ .

This comparison is shown in Fig. 2(a) for  $\rho_p/\rho_f = 0.001$  and  $Ar = 28900$  which results in a terminal Reynolds number of  $Re = 290$ . For the comparison, the gravitational velocity and time scale are utilized as reference values:

$$u_g = \sqrt{|\rho_p/\rho_f - 1|gd_p}, \quad t_g = \sqrt{\frac{d_p}{|\rho_p/\rho_f - 1|g}}.$$

The results of PUREIBM are shown for two different grid resolutions in this figure. It is clear that at early time the PUREIBM results match very well with the reference result of Dušek's group. However, the terminal velocity is slightly different. The difference decreases with increasing the grid resolution but convergence to the reference result is slow. Similarly, the IBM results of Schwarz et al. [45] deviates from the reference terminal velocity. In IBM, the no-slip and no-penetration velocity boundary conditions on the particle surface are imposed on Lagrangian marker points through the immersed boundary force, which is computed at the Lagrangian marker points and then spread to the Cartesian grid using a regularized delta function. In the implementation of IBM that is used by Schwarz et al. [45], the Lagrangian marker points are

on the surface of the particle and the immersed boundary force spread is into the fluid domain, while in PReIBM the Lagrangian marker points are inside the particle and the immersed boundary force is restricted to Eulerian grid points lying inside the sphere while the fluid domain is uncontaminated by the immersed boundary force. This could explain why the terminal velocity results of Schwarz et al. [45] are smaller than the reference data and the results of PReIBM are larger.

In Fig. 2(b), the particle rise velocity for  $D_m = 80$  and different time step is plotted to show that the velocity converges with decreasing time step. In this figure, also the time step is constant since the CFL number is always smaller than maximum CFL. The smallest time step  $\Delta t = 0.0004$  is used in Fig. 2(a). Also, note that only the beginning of the acceleration phase is considered for comparison in Fig. 2, which is before the particle path shows oscillations. When the Reynolds number is higher than 135 (as here) and the particle density is much smaller than that of surrounding fluid, the particle motion is spiral and the drag coefficient is a constant, equal to 0.95 [60, 61]. At Reynolds number below 135, the drag coefficient follows the standard drag curve and the trajectory is linear [60]. This behavior is explained as the mechanical inertia of the particle becomes small enough for the wake to induce rotation of the particle, thus creating a spiral trajectory [60]. In addition, the dominating inertial force is the added mass from the attached fluid mass for light particles which is accelerated with the particle. This effect is shown recently to play an important role in the dynamics of buoyant particles suspensions [55, 62]. On the other hand for heavy particles, the particle dynamics are mainly governed by the inertia of the immersed body itself.

### 5.1.2. Drag coefficient

As another validation, the results of PReIBM for the drag coefficient of a single rising particle are compared with the experimental results of [8]. The experimental work reports the drag of nearly spherical gaseous bubbles (aspect ratio  $E > 0.95$ ) in tap (contaminated) water. As explained already, buoyant

particles are a good approximation for bubbles in contaminated liquid, so this comparison is valid.

Additionally, the results are compared with the drag correlation for a single bubble in contaminated liquid [63]. This correlation is expressed as:

$$C_D = \max \left[ \frac{24}{Re} (1 + 0.15Re^{0.687}), \frac{8}{3} \frac{Eo}{Eo + 4} \right], \quad (29)$$

where  $Eo$  is Eötvös number which represents the ratio between buoyancy and surface tension forces and is defined as,

$$Eo = \frac{g(\rho_f - \rho_p) d_p^2}{\sigma}, \quad (30)$$

with  $\sigma$  being the surface tension. Note that  $Eo$  for rigid particles correspond to  $\sigma \rightarrow \infty$ , so  $Eo$  is zero in our simulations.

The simulation setup is similar to the previous case (section 5.1.1) with  $\rho_p/\rho_f = 0.001$  and different  $Ar$  to achieve different Reynolds number defined by terminal velocity. Figure 3 shows the comparison of PReIBM results with experimental results and the drag correlation in Eq. (29). The results of PReIBM are presented for two grid resolutions and it is clear that at higher Reynolds number the finer grid gives the correct results. In general, the results of PReIBM match very well with experiments and the correlation. Note that the Reynolds number here is smaller than 135, and as mentioned earlier, in this range the buoyant particle drag follows the standard drag curve.

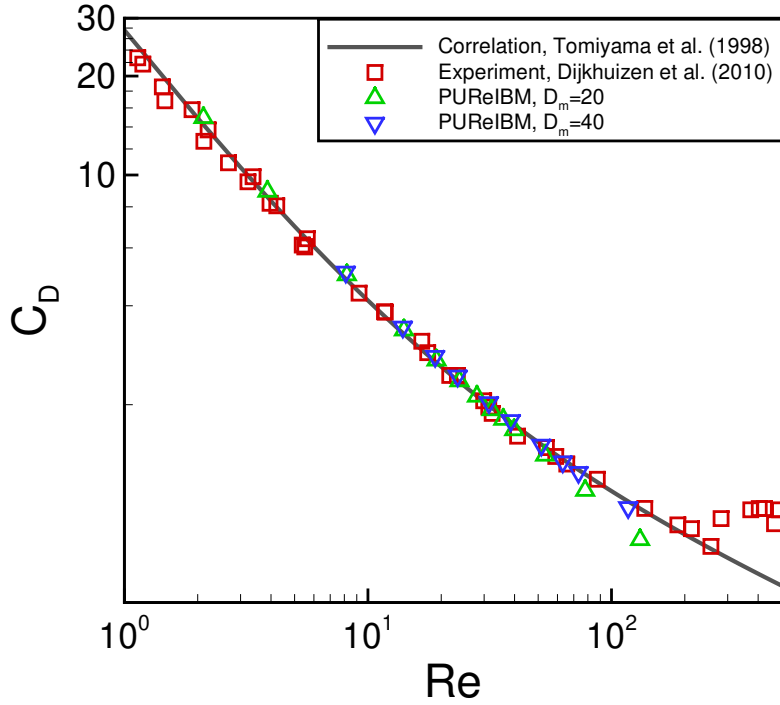


Figure 3: Drag coefficient versus Reynolds number from simulation of a single buoyant particle in PUnReIBM compared with experimental results of a nearly spherical bubble in contaminated [8] liquid and correlation of drag on a single bubble in contaminated liquid [63].

### 5.2. Rise of two buoyant particles

The next simulation that is presented is for the rising of two in-line particles. The particles rising in-line is a specific but typical case where mutual interactions between particles are evident. In this particular case, the rise velocity of the trailing particle is affected (and increased) by the wake of the leading particle and finally, the trailing particle reaches the leading particle.

The simulation is again performed in a cuboidal domain with periodic boundary conditions in all directions. The length of the domain in the direction of gravity is  $L_x = 89.6d_p$  which is 14 times the length of the domain in other directions. Similar to the single particle case, the particles rise due to the gravitational force. The simulation is performed for a case where  $Ar = 1700$ ,  $\rho_p/\rho_f = 0.001$ ,  $C_v = 0.15$ , and the initial surface-to-surface distance between

particles is  $h_0/d_p = 11.6$ . Figure 4(a) shows the rise velocity of particles versus surface-to-surface distance between them. The experimental results of Katz and Meneveau [64] for a similar case, but for bubbles in distilled water is also shown in this figure. For both the numerical and experimental cases, the Reynolds number based on the terminal velocity of single particle/bubbles is 35.4. Although the trend of the rise velocity in both cases is similar, they do not match. One reason for this is that the results of PUnReIBM represent bubbles in contaminated liquid while the experimental results are for bubbles in clean liquid. Note that Katz and Meneveau [64] used commercially available distilled water and not highly purified liquid which could also be considered a partially contaminated liquid. Nevertheless, it is known that the drag force, and consequently the rise velocity, of bubbles in clean, partially contaminated, or contaminated is different. To have a better comparison, the rise velocity scaled with the rise velocity of a single particle/bubble is plotted in Fig, 4(b). This figure shows that the behavior of bubbles in contaminated or clean liquid is comparable if a proper scaling is used.

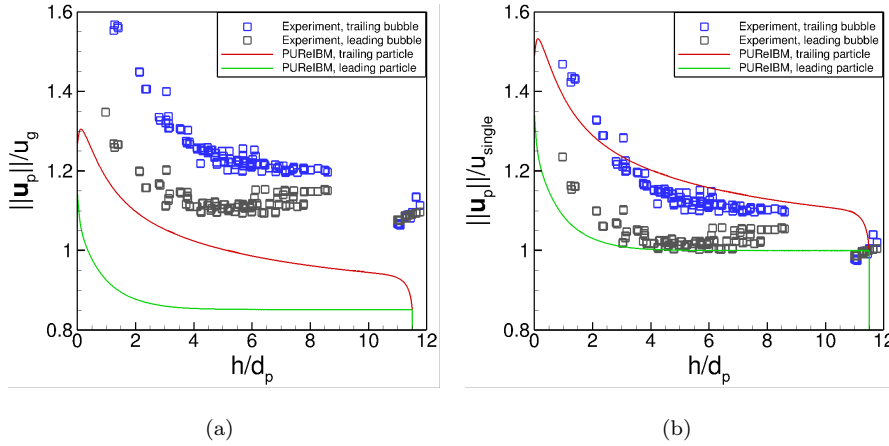


Figure 4: Rise velocity of two in-line particles from simulation in PUnReIBM compared with experimental results of two in-line bubbles in distilled water [64]. (a) Rise velocity is scaled with the gravitational velocity. (b) Rise velocity is scaled with the rise velocity of a single particle/bubble.

### 5.3. Simulation of bubbly flows: an illustrative example

The main goal of this paper is to perform the simulation of bubbly flows at high volume fractions. In this section, the results of simulations for bubbly flows in contaminated liquid at volume fraction 0.1 to 0.4 is presented and in particular, the drag force on the swarm is discussed.

The simulations are performed in a cubic domain with periodic boundary conditions. The length of the domain  $L$  is chosen to ensure that the two-point correlation functions in the fluid phase decay to zero within the box length [52]. The initial positions of the particles are obtained following elastic collisions (in the absence of interstitial fluid) starting from a lattice arrangement with a Maxwellian velocity distribution. The particles and fluid are initially at rest and evolve under the action of gravity. The simulations are carried out until the mean particle velocity reaches a statistically stationary state. In our simulations, the mean drag on particles is computed by averaging over all particles and then ensemble-averaging over different particle configurations. For each case, five independent realizations (corresponding to a specified initial particle configuration) are simulated in this study.

The salient numerical and physical parameters used in the simulations are reported in Table 2. The grid resolution used in this study is the same as our previous works [52, 55] which we have shown is sufficient to obtain converged results for the mean drag and second moments of velocity. The simulations are performed for  $\rho_p/\rho_f = 0.001$  and at four different volume fractions. Since an increase in volume fraction decreases the rising velocity, the Archimedes number is also increased by increasing the volume fraction. As a result, the Reynolds number

$$Re_m = \frac{(1 - \phi) |\langle \mathbf{W} \rangle| d_p}{\nu_f}$$

reaches a constant value of  $Re_m = 20$ . In the definition of Reynolds number,  $|\langle \mathbf{W} \rangle|$  is the mean slip velocity between the particles and the fluid.

Table 2: The numerical and physical parameters of the simulations: volume fraction of particles  $\phi$ , the number of grid cells across the diameter of a particle  $d_p/\Delta x$ , the ratio of the length of the box to the particle diameter  $L/d_p$ , number of particles  $N_p$ , Archimedes number  $Ar$ , and particle-to-fluid density ratio  $\rho_p/\rho_f$ .

| $\phi$ | $d_p/\Delta x$ | $L/d_p$ | $N_p$ | $Ar$ | $\rho_p/\rho_f$ |
|--------|----------------|---------|-------|------|-----------------|
| 0.1    | 20             | 10.08   | 200   | 1600 | 0.001           |
| 0.2    | 20             | 8.06    | 200   | 2800 | 0.001           |
| 0.3    | 30             | 7.05    | 200   | 4900 | 0.001           |
| 0.4    | 30             | 6.4     | 200   | 9400 | 0.001           |

According to Eq. (11),  $C_v^{min}$  is related to the added mass coefficient. Many studies have shown that added mass coefficient increases with volume fraction [16, 65–68]. Spelt and Sangani [69] also reported the same dependence, however, they included the effect of microstructure on the added mass through the velocity fluctuations of bubbles. On the other hand, Simcik et al. [46] and Simcik and Ruzicka [70] have reported that the added mass coefficient can decrease or increase with volume fraction depending on the shape of the computational domain. In our simulations,  $C_v^{min}$  should increase with volume fraction to get stable results which indicates that the added mass coefficient increases with volume fraction.

In PUReIBM,  $C_v^{min}$  is found from numerical experiments to increase from 0.18 for  $\phi = 0.1$  to 0.22 for  $\phi = 0.4$ . Using the correlation by Zuber [65],  $C_{am}$  increases from 0.66 for  $\phi = 0.1$  to  $C_{am} = 1.5$  for  $\phi = 0.4$ . It shows that the growth of  $C_v^{min}$  with volume fraction is slower than the growth of  $C_{am}$ . In this study,  $C_v = 0.25$  is used for all volume fractions in the simulation of particle suspensions. It is also important to mention that there is no added mass effect in an average sense since the simulations reach a statistically stationary state, however, each individual particle experiences the added mass effect. Therefore, using virtual force stabilization is necessary at any stage of the simulations.

The results presented in this section are the drag force on bubbly flows in

contaminated liquid obtained from PUREIBM which are compared with experimental and numerical results. The drag coefficient for the swarm is defined as:

$$\frac{C_D}{C_{D,\infty}(1-\phi)} = f(\phi, Eo), \quad (31)$$

where  $C_{D,\infty}$  is the drag on a single bubble in an infinite domain.

As discussed in section 5.2, the drag of bubbles in clean and contaminated liquid is not comparable unless a proper scaling is used. For this reason, different studies have used  $C_{D,\infty}$  from different correlations or measurements in Eq. (31) for reporting  $f(\phi, Eo)$ . In this work, Eq. (29) is used for  $C_{D,\infty}$ .

All the experimental correlations used in this paper for comparison only depend on the volume fraction (see Table 3) while the numerical correlations depend on both volume fraction and Eötvös number (see Table 4). The numerical correlations are obtained from FR-DNS using the front-tracking method (FTM) and three different correlations are proposed based on the range of applicability. The results in this section are compared with the third correlation since it is developed for the range of parameter in which bubbles are spherical or ellipsoidal so it is expected to match better with the results in this work which simulates spherical bubbles.

Table 3: Experimental correlations for the scaled drag coefficient, i.e., function  $f$  in Eq. (31).

| Correlation  | Condition     | Reference                    |
|--|---------------|------------------------------|
| $\left[(1-\phi)^{1.39}\right]^{-2}$                | $\phi < 0.2$  | Bridge et al. [71]           |
| $\left[(1-\phi)^{1.39} (1+2.55\phi^3)\right]^{-2}$ | $\phi < 0.66$ | Lockett and Kirkpatrick [72] |
| $\exp(3.64\phi) + \phi^{0.864}$                    | $\phi < 0.45$ | Rusche and Issa [73]         |

Table 4: Numerical correlations for the scaled drag coefficient, i.e., function  $f$  in Eq. (31).

| Correlation  | Condition                                | Reference           |
|--|--|---------------------|
| $1 + \left(\frac{18}{Eo}\right) \phi$              | wobbling bubbles                         | Roghair et al. [74] |
|  | $1.2 < Eo < 4.8$<br>$0.05 < \phi < 0.45$ |                     |
| $1 + \left(\frac{22}{Eo + 0.4}\right) \phi$        | wobbling bubbles                         | Roghair et al. [75] |
|  | $0.6 < Eo < 4.8$<br>$0.05 < \phi < 0.4$  |                     |
| $1 + \left(\frac{6.612Eo + 2.023}{Eo}\right) \phi$ | spherical/ellipsoidal bubbles            | Roghair et al. [75] |
|  | $0.5 < Eo < 2$<br>$0.05 < \phi < 0.15$   |                     |

Figure 5 compares the results for the scaled drag coefficient in bubbly flows. The correlations are extended to higher volume fractions if the range for which they are proposed covers a smaller range. The scaled drag coefficient for contaminated bubbles (using PReIBM) matches very well with the FR-DNS results of FTM [75] for clean bubbles at  $Eo = 0.5$  at volume fractions 0.1 and 0.2. At this  $Eo$ , the bubbles are spherical while at higher values they become ellipsoidal. For higher volume fractions ( $\phi = 0.3, 0.4$ ), the results of contaminated bubbles (using PReIBM) and clean bubbles (using FTM [75]) do not match very well. One possible reason is that Roghair’s third correlation is proposed for  $0.05 < \phi < 0.15$  and it might not be valid for higher volume fractions. Nevertheless, it is interesting to note that the results of PReIBM, similar to the experimental correlations, show a nonlinear dependence of drag coefficient on volume fraction while all correlations of clean bubbles using FTM have linear dependence (see Table 4). Although Roghair et al. [74] do not provide the reason behind the linear nature of their correlations, they raise four possible issues in their work including the effect of 1) contamination, 2) coalescence and breakup, 3) normalization with  $C_{D,\infty}$  which comes from different correlations or measurements for each case, and 4) having smaller computational domain in

comparison to large domain of experiments.

Among these, two limitations are addressed in this work. First, the bubbles in this study are contaminated bubbles and the results of experimental works might have also had some level of contamination. Secondly, the FR-DNS results from FTM by Roghair et al. [74, 75] can only take local gas fractions into account, since the computational domain is small compared to the physical domain typically used in experiments. In fact, Roghair et al. [74, 75] have 16 up to 32 bubbles for different simulations while in PReIBM 200 particles is used for each case. Therefore, it is concluded that PReIBM results have a similar trend to experiments since both of them take into account the global volume fraction.

It should also be mentioned that Simonnet et al. [76] developed a drag correlation using local volume fraction definition in their experiments but their correlation predicts that drag coefficient increases very slowly up to volume fraction 15% and then decreases with increasing volume fraction. The main reason for the different behavior they obtained is that the bubbles in their experiment are large and because of this their correlation is not presented here [76]. Gillissen et al. [77] have also reported the drag of bubble swarms using the correlation of drag coefficient for a single bubble with an effective viscosity in their definition of Reynolds number. Following this approach, the scaled drag coefficient (Eq. (31)) will depend on Reynolds number unlike the other correlations presented in Tables 3 and 4, so Gillissen's correlation is also not used here for comparison.

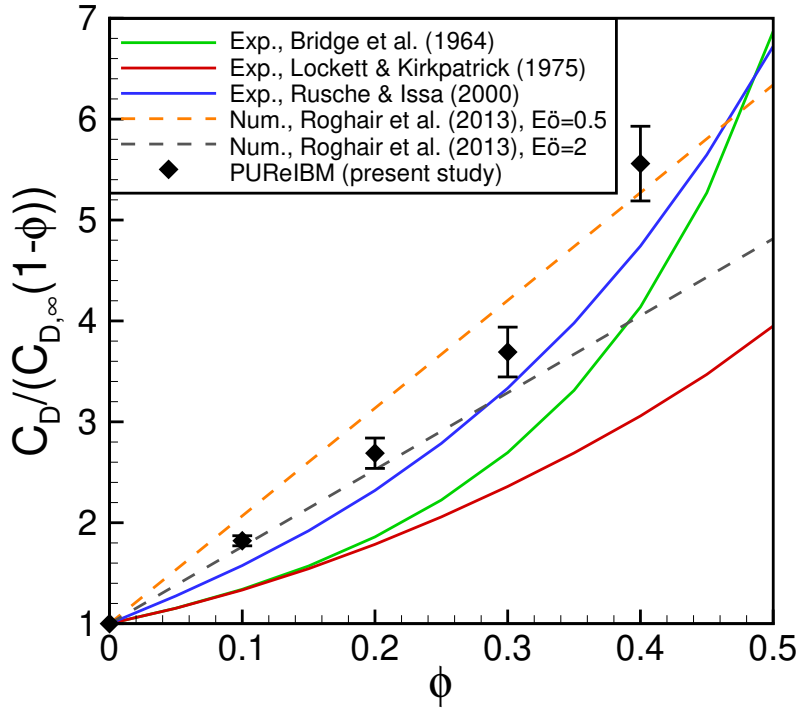


Figure 5: Comparison of scaled drag coefficient obtained from PURelBM with different drag correlations. Solid lines are the correlations obtained from different experiments. Dashed lines are the correlation obtained from simulations using FTM [75] for two different values of  $E\ddot{o}$ . Symbols are the scaled drag coefficients obtained from PURelBM (present study). The error bars represent 95% confidence intervals.

## 6. Conclusions

In this work, an accurate, convergent, and stable FR-DNS solver based on PURelBM is developed for simulation of bubbles in contaminated liquid with a density ratio as small as 0.001 and for a range of volume fraction up to 40%. It is explained that when the mass of a bubble or particle is smaller than the added mass induced by the surrounding fluid, explicit numerical methods are unstable. To stabilize the method, the virtual force technique introduced by Schwarz et al. [45] is generalized and extended. It is shown that the virtual force constant  $C_v$  has a lower limit which depends on the density ratio, the added mass coefficient,

and the numerical method. Since the added mass coefficient increases with an increase in the volume fraction of bubbles, it is concluded that  $C_v$  should also increase in the case of bubble swarm when compared to the single bubble case.

Simulations of a single rising particle at different Archimedes number are presented and compared with the numerical and experimental reference data to validate the implementation of the virtual force in PReIBM. Then two in-line rising particles are simulated and compared with experimental results. Finally, simulations of dense bubbly flows in contaminated liquid are presented. The scaled drag coefficient of bubble swarms at different volume fractions are compared with numerical and experimental correlations from the literature. It is shown the increase in scaled drag coefficient of contaminated bubble swarms with volume fraction from FR-DNS using PReIBM matches the nonlinear trend in experimental data, while the correlations from FR-DNS using FTM by Roghair et al. [74, 75] predict a linear increase. They hypothesized that this linear dependence could be to the fact that their bubbles are in clean liquid and their simulations are performed for a small domain with 16 up to 32 bubbles in it. It is shown here that considering a larger domain with 200 bubbles in contaminated liquid predicts the nonlinear behavior seen in experimental studies.

### **Acknowledgments**

This material is based upon work supported by the National Science Foundation under Grant No. 1438143.

### **Appendix A. Description of numerical methods used for solving model equation**

As explained in section 3.2, to solve Eq. (13), one needs to numerically calculate  $du_p/dt$  on the RHS and then numerically integrate the equation to calculate  $u_p$  in time. In this Appendix, different numerical methods that are

used for solving Eq. (13) are explained. Eq. (13) can be written as:

$$\frac{du_p}{dt} = c_u u_p + c_g g + c_a \frac{du_p}{dt}, \quad (\text{A.1})$$

where

$$c_u = -\frac{18\mu_f}{d_p^2(\rho_p + C_v\rho_f)}, \quad c_g = \frac{\rho_p - \rho_f}{(\rho_p + C_v\rho_f)}, \quad c_a = \frac{(C_v - C_{am})\rho_f}{(\rho_p + C_v\rho_f)}.$$

For the calculation of  $F_a = c_a du_p/dt$ , the following methods can be used:

- 1st-order backward finite difference (1st order BW)

$$F_a^n = c_a \frac{u^n - u^{n-1}}{\Delta t} \quad (\text{A.2})$$

- 2nd-order backward finite difference (2nd order BW)

$$F_a^n = c_a \frac{3u^n - 4u^{n-1} + u^{n-2}}{2\Delta t} \quad (\text{A.3})$$

- 3rd-order backward finite difference (3rd order BW)

$$F_a^n = c_a \frac{11u^n - 18u^{n-1} + 9u^{n-2} - 2u^{n-3}}{6\Delta t} \quad (\text{A.4})$$

- Adams-Bashforth-predictor scheme (AB-predictor)

$$\begin{aligned} F_a^n &= c_a \frac{3u^n - 4u^{n-1} + u^{n-2}}{2\Delta t} \\ \tilde{f}^n &= c_u u^n + c_g g + F_a^n \\ u_{pred}^{n+1} &= u^n + \frac{\Delta t}{2} (3\tilde{f}^n - \tilde{f}^{n-1}) \\ F_{a,pred}^{n+1} &= c_a \frac{3u_{pred}^{n+1} - 4u^n + u^{n-1}}{2\Delta t} \\ F_a^{n+\frac{1}{2}} &= \frac{1}{2} (F_a^n + F_{a,pred}^{n+1}) \end{aligned} \quad (\text{A.5})$$

For integrating Eq. (A.1) to calculate  $u_p$ , the following methods can be used:

- Euler (1st order accurate)

$$\begin{aligned} \tilde{f}^n &= c_u u^n + c_g g + F_a^n \\ u^{n+1} &= u^n + \Delta t \tilde{f}^n \end{aligned} \quad (\text{A.6})$$

- 2nd-order Adams-Bashforth (2nd order accurate)

$$\begin{aligned}\tilde{f}^n &= c_u u^n + c_g g + F_a^n \\ u^{n+1} &= u^n + \frac{\Delta t}{2} (3\tilde{f}^n - \tilde{f}^{n-1})\end{aligned}\tag{A.7}$$

- 3rd-order Runge-Kutta (3rd order accurate)

The coefficients are chosen similar to the work of Wray [78].

$$\begin{aligned}k_1 &= c_u u^n + c_g g + F_a^n \\ k_2 &= c_u \left( u^n + \frac{8}{15} k_1 \Delta t \right) + c_g g + F_a^n \\ k_3 &= c_u \left( u^n + \frac{1}{4} k_1 \Delta t + \frac{5}{12} k_2 \Delta t \right) + c_g g + F_a^n \\ u^{n+1} &= u^n + \Delta t \left( \frac{1}{4} k_1 + \frac{3}{4} k_3 \right)\end{aligned}\tag{A.8}$$

## Appendix B. Results from generalized approach of virtual force concept

As we discussed in section 3.3.1, in the generalized approach,  $C_v$  will change from one particle to another. In practice the value of  $m_v$ , and consequently  $C_v$ , sometimes becomes negative. To solve this problem with the negative values of  $C_v$ , one idea is to limit the  $C_v$  from Eq. (18) with  $C_v^{min}$  of a single particle. A comparison of the results for a case with  $\phi = 0.4$  obtained with constant  $C_v = 0.25$  and a case with variable  $C_v$  with the limit of  $C_v^{min} = 0.15$  is done in Fig. B.6. This figure shows that with variable  $C_v$  the mean drag force oscillates unlike the constant  $C_v$  case.

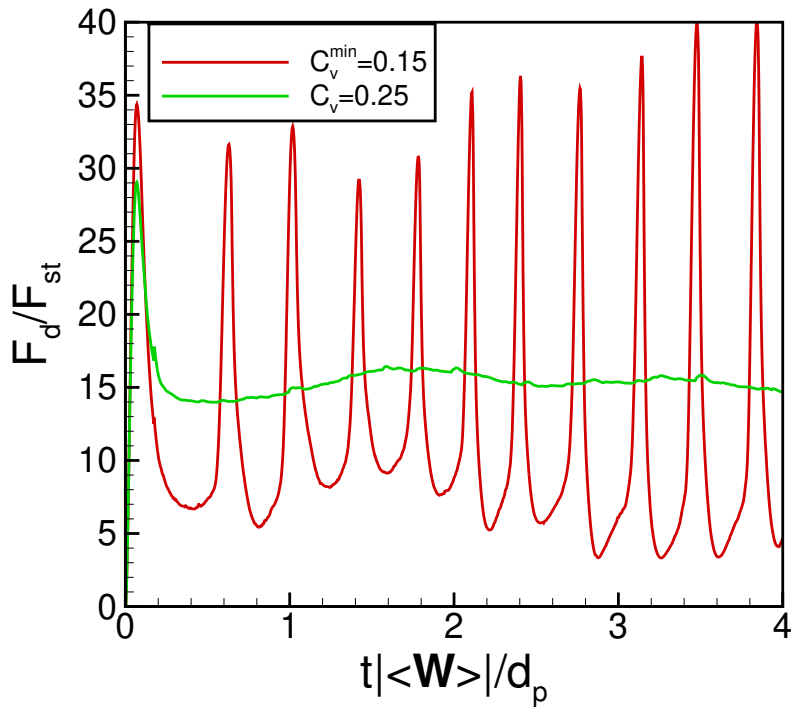


Figure B.6: Comparison of the results from simulations with constant  $C_v = 0.25$  and variable  $C_v$  with  $C_v^{\min} = 0.15$ .

## References

## References

1. Tenneti S, Subramaniam S. Particle-resolved direct numerical simulation for gas–solid flow model development. *Annu Rev Fluid Mech* 2014;46(1):199–230. doi:10.1146/annurev-fluid-010313-141344.
2. Clift R, Grace JR, Weber ME. Bubbles, drops, and particles. New York: Academic Press; 1978.
3. Magnaudet J, Eames I. The motion of high-Reynolds-number bubbles in inhomogeneous flows. *Annu Rev Fluid Mech* 2000;32(1):659–708. doi:10.1146/annurev.fluid.32.1.659.

4. Takagi S, Matsumoto Y. Surfactant effects on bubble motion and bubbly flows. *Annu Rev Fluid Mech* 2011;43(1):615–36. doi:10.1146/annurev-fluid-122109-160756.
5. Sridhar G, Katz J. Drag and lift forces on microscopic bubbles entrained by a vortex. *Phys Fluids* 1995;7(2):389–99. doi:10.1063/1.868637.
6. Bel Fdhila R, Duineveld PC. The effect of surfactant on the rise of a spherical bubble at high Reynolds and Peclet numbers. *Phys Fluids* 1996;8(2):310–21. doi:10.1063/1.868787.
7. Cartellier A, Rivière N. Bubble-induced agitation and microstructure in uniform bubbly flows at small to moderate particle Reynolds numbers. *Phys Fluids* 2001;13(8):2165–81. doi:10.1063/1.1381562.
8. Dijkhuizen W, Roghair I, Annaland MVS, Kuipers J. DNS of gas bubbles behaviour using an improved 3D front tracking model—Drag force on isolated bubbles and comparison with experiments. *Chem Eng Sci* 2010;65(4):1415–26. doi:10.1016/j.ces.2009.10.021.
9. Peters F, Els C. An experimental study on slow and fast bubbles in tap water. *Chem Eng Sci* 2012;82:194–9. doi:10.1016/j.ces.2012.06.061.
10. Ryskin G, Leal LG. Numerical solution of free-boundary problems in fluid mechanics. Part 1. The finite-difference technique. *J Fluid Mech* 1984;148:1–17. doi:10.1017/S0022112084002214.
11. Tomiyama A, Zun I, Sou A, Sakaguchi T. Numerical analysis of bubble motion with the VOF method. *Nucl Eng Des* 1993;141(1):69–82. doi:10.1016/0029-5493(93)90093-0.
12. Chen L, Garimella SV, Reizes JA, Leonardi E. The development of a bubble rising in a viscous liquid. *J Fluid Mech* 1999;387:61–96. doi:10.1017/S0022112099004449.

13. van Sint Annaland M, Deen N, Kuipers J. Numerical simulation of gas bubbles behaviour using a three-dimensional volume of fluid method. *Chem Eng Sci* 2005;60(11):2999–3011. doi:10.1016/j.ces.2005.01.031.
14. Nagrath S, Jansen KE, Lahey RT. Computation of incompressible bubble dynamics with a stabilized finite element level set method. *Comput Methods Appl Mech Eng* 2005;194(42):4565–87. doi:10.1016/j.cma.2004.11.012.
15. Bolotnov IA, Jansen KE, Drew DA, Oberai AA, Lahey RT, Podowski MZ. Detached direct numerical simulations of turbulent two-phase bubbly channel flow. *Int J Multiphase Flow* 2011;37(6):647–59. doi:10.1016/j.ijmultiphaseflow.2011.03.002.
16. Sankaranarayanan K, Shan X, Kevrekidis IG, Sundaresan S. Analysis of drag and virtual mass forces in bubbly suspensions using an implicit formulation of the lattice Boltzmann method. *J Fluid Mech* 2002;452:61–96. doi:10.1017/S0022112001006619.
17. Yin X, Koch DL. Lattice-Boltzmann simulation of finite Reynolds number buoyancy-driven bubbly flows in periodic and wall-bounded domains. *Phys Fluids* 2008;20(10):103304. doi:10.1063/1.3001728.
18. Unverdi SO, Tryggvason G. A front-tracking method for viscous, incompressible, multi-fluid flows. *J Comput Phys* 1992;100(1):25–37. doi:10.1016/0021-9991(92)90307-K.
19. Kempe T, Lennartz M, Schwarz S, Fröhlich J. Imposing the free-slip condition with a continuous forcing immersed boundary method. *J Comput Phys* 2015;282:183–209. doi:10.1016/j.jcp.2014.11.015.
20. Cuenot B, Magnaudet J, Spennato B. The effects of slightly soluble surfactants on the flow around a spherical bubble. *J Fluid Mech* 1997;339:25–53. doi:10.1017/S0022112097005053.

21. Muradoglu M, Tryggvason G. A front-tracking method for computation of interfacial flows with soluble surfactants. *J Comput Phys* 2008;227(4):2238–62. doi:10.1016/j.jcp.2007.10.003.
22. Santarelli C, Fröhlich J. Direct numerical simulations of spherical bubbles in vertical turbulent channel flow. *Int J Multiphase Flow* 2015;75:174–93. doi:10.1016/j.ijmultiphaseflow.2015.05.007.
23. Inamuro T, Ogata T, Tajima S, Konishi N. A lattice Boltzmann method for incompressible two-phase flows with large density differences. *J Comput Phys* 2004;198(2):628–44. doi:10.1016/j.jcp.2004.01.019.
24. Tryggvason G, Bunner B, Esmaeeli A, Juric D, Al-Rawahi N, Tauber W, Han J, Nas S, Jan YJ. A front-tracking method for the computations of multiphase flow. *J Comput Phys* 2001;169(2):708–59. doi:10.1006/jcph.2001.6726.
25. Dijkhuizen W, Roghair I, Annaland MVS, Kuipers J. DNS of gas bubbles behaviour using an improved 3D front tracking model—Model development. *Chem Eng Sci* 2010;65(4):1427–37. doi:10.1016/j.ces.2009.10.022.
26. Uhlmann M. An immersed boundary method with direct forcing for the simulation of particulate flows. *J Comput Phys* 2005;209(2):448–76. doi:10.1016/j.jcp.2005.03.017.
27. Kempe T, Fröhlich J. An improved immersed boundary method with direct forcing for the simulation of particle laden flows. *J Comput Phys* 2012;231(9):3663–84. doi:10.1016/j.jcp.2012.01.021.
28. Breugem WP. A second-order accurate immersed boundary method for fully resolved simulations of particle-laden flows. *J Comput Phys* 2012;231(13):4469–98. doi:10.1016/j.jcp.2012.02.026.

29. Yang J, Stern F. A sharp interface direct forcing immersed boundary approach for fully resolved simulations of particulate flows. *ASME J Fluids Eng* 2014;136(4):040904. doi:10.1115/1.4026198.
30. Maxey M. Simulation methods for particulate flows and concentrated suspensions. *Annu Rev Fluid Mech* 2017;49(1):171–93. doi:10.1146/annurev-fluid-122414-034408.
31. Causin P, Gerbeau J, Nobile F. Added-mass effect in the design of partitioned algorithms for fluid–structure problems. *Comput Methods Appl Mech Eng* 2005;194(42):4506–27. doi:10.1016/j.cma.2004.12.005.
32. Förster C, Wall WA, Ramm E. Artificial added mass instabilities in sequential staggered coupling of nonlinear structures and incompressible viscous flows. *Comput Methods Appl Mech Eng* 2007;196(7):1278–93. doi:10.1016/j.cma.2006.09.002.
33. Borazjani I, Ge L, Sotiropoulos F. Curvilinear immersed boundary method for simulating fluid structure interaction with complex 3D rigid bodies. *J Comput Phys* 2008;227(16):7587–620. doi:10.1016/j.jcp.2008.04.028.
34. Sotiropoulos F, Yang X. Immersed boundary methods for simulating fluid–structure interaction. *Prog Aerosp Sci* 2014;65:1–21. doi:10.1016/j.paerosci.2013.09.003.
35. Hu HH, Patankar N, Zhu M. Direct numerical simulations of fluid–solid systems using the arbitrary Lagrangian–Eulerian technique. *J Comput Phys* 2001;169(2):427–62. doi:10.1006/jcph.2000.6592.
36. Fernández MÁ, Moubachir M. A Newton method using exact jacobians for solving fluid–structure coupling. *Comput Struct* 2005;83(2):127–42. doi:10.1016/j.compstruc.2004.04.021; Advances in Analysis of Fluid Structure Interaction.
37. Figueroa CA, Vignon-Clementel IE, Jansen KE, Hughes TJ, Taylor CA. A coupled momentum method for modeling blood flow in three-dimensional

- deformable arteries. *Comput Methods Appl Mech Eng* 2006;195(41):5685–706. doi:10.1016/j.cma.2005.11.011; John H. Argyris Memorial Issue. Part II.
38. Tallec PL, Mouro J. Fluid structure interaction with large structural displacements. *Comput Methods Appl Mech Eng* 2001;190(24):3039–67. doi:10.1016/S0045-7825(00)00381-9; Advances in Computational Methods for Fluid–Structure Interaction.
39. Burman E, Fernández MA. Stabilization of explicit coupling in fluid–structure interaction involving fluid incompressibility. *Comput Methods Appl Mech Eng* 2009;198(5):766–84. doi:10.1016/j.cma.2008.10.012.
40. Guidoboni G, Glowinski R, Cavallini N, Canic S. Stable loosely-coupled-type algorithm for fluid–structure interaction in blood flow. *J Comput Phys* 2009;228(18):6916–37. doi:10.1016/j.jcp.2009.06.007.
41. Garg R, Tenneti S, Mohd-Yusof J, Subramaniam S. Direct numerical simulation of gas–solids flow based on the immersed boundary method. In: Pannala S, Syamlal M, O’Brien TJ, eds. *Computational Gas–Solids Flows and Reacting Systems: Theory, Methods and Practice*. Hershey, PA: IGI Global; 2011:245–76. doi:10.4018/978-1-61520-651-3.ch008.
42. Tenneti S, Garg R, Hrenya C, Fox R, Subramaniam S. Direct numerical simulation of gas–solid suspensions at moderate Reynolds number: quantifying the coupling between hydrodynamic forces and particle velocity fluctuations. *Powder Technol* 2010;203(1):57–69. doi:10.1016/j.powtec.2010.03.042.
43. Yang J, Stern F. A non-iterative direct forcing immersed boundary method for strongly-coupled fluid–solid interactions. *J Comput Phys* 2015;295:779–804. doi:10.1016/j.jcp.2015.04.040.
44. Tschisgale S, Kempe T, Fröhlich J. A non-iterative immersed boundary

- method for spherical particles of arbitrary density ratio. *J Comput Phys* 2017;339:432–52. doi:10.1016/j.jcp.2017.03.026.
45. Schwarz S, Kempe T, Fröhlich J. A temporal discretization scheme to compute the motion of light particles in viscous flows by an immersed boundary method. *J Comput Phys* 2015;281:591–613. doi:10.1016/j.jcp.2014.10.039.
  46. Simcik M, Ruzicka M, Drahoš J. Computing the added mass of dispersed particles. *Chem Eng Sci* 2008;63(18):4580–95. doi:10.1016/j.ces.2008.06.011.
  47. Tenneti S, Mehrabadi M, Subramaniam S. Stochastic Lagrangian model for hydrodynamic acceleration of inertial particles in gas–solid suspensions. *J Fluid Mech* 2016;788:695–729. doi:10.1017/jfm.2015.693.
  48. Akiki G, Jackson TL, Balachandar S. Force variation within arrays of monodisperse spherical particles. *Phys Rev Fluids* 2016;1:044202. doi:10.1103/PhysRevFluids.1.044202.
  49. Esteghamatian A, Euzenat F, Hammouti A, Lance M, Wachs A. A stochastic formulation for the drag force based on multiscale numerical simulation of fluidized beds. *Int J Multiphase Flow* 2018;99:363–82. doi:10.1016/j.ijmultiphaseflow.2017.11.003.
  50. Mohd-Yusof J. Interaction of massive particles with turbulence. Ph.D. thesis; Cornell University; 1996.
  51. Mehrabadi M, Tenneti S, Garg R, Subramaniam S. Pseudo-turbulent gas-phase velocity fluctuations in homogeneous gas–solid flow: fixed particle assemblies and freely evolving suspensions. *J Fluid Mech* 2015;770:210–46. doi:10.1017/jfm.2015.146.
  52. Tenneti S, Garg R, Subramaniam S. Drag law for monodisperse gas–solid systems using particle-resolved direct numerical simulation of flow past

- fixed assemblies of spheres. *Int J Multiphase Flow* 2011;37(9):1072–92. doi:10.1016/j.ijmultiphaseflow.2011.05.010.
53. Cundall PA, Strack ODL. A discrete numerical model for granular assemblies. *Géotechnique* 1979;29(1):47–65. doi:10.1680/geot.1979.29.1.47.
54. Akiki G, Moore W, Balachandar S. Pairwise-interaction extended point-particle model for particle-laden flows. *J Comput Phys* 2017;351:329–57. doi:10.1016/j.jcp.2017.07.056.
55. Tavanashad V, Passalacqua A, Fox RO, Subramaniam S. Effect of density ratio on velocity fluctuations in dispersed multiphase flow from simulations of finite-size particles. *Acta Mech* 2019;230:469–84. doi:10.1007/s00707-018-2267-3.
56. Simeonov JA, Calantoni J. Modeling mechanical contact and lubrication in direct numerical simulations of colliding particles. *Int J Multiphase Flow* 2012;46:38–53. doi:10.1016/j.ijmultiphaseflow.2012.05.008.
57. Sierakowski AJ, Prosperetti A. Resolved-particle simulation by the Physalis method: enhancements and new capabilities. *J Comput Phys* 2016;309:164–84. doi:10.1016/j.jcp.2015.12.057.
58. Jenny M, Dušek J. Efficient numerical method for the direct numerical simulation of the flow past a single light moving spherical body in transitional regimes. *J Comput Phys* 2004;194(1):215–32. doi:10.1016/j.jcp.2003.09.004.
59. Jenny M, Dušek J, Bouchet G. Instabilities and transition of a sphere falling or ascending freely in a Newtonian fluid. *J Fluid Mech* 2004;508:201–39. doi:10.1017/S0022112004009164.
60. Karamanev DG, Chavarie C, Mayer RC. Dynamics of the free rise of a light solid sphere in liquid. *AIChE J* 1996;42(6):1789–92. doi:10.1002/aic.690420630.

61. Horowitz M, Williamson CHK. The effect of Reynolds number on the dynamics and wakes of freely rising and falling spheres. *J Fluid Mech* 2010;651:251–94. doi:10.1017/S0022112009993934.
62. Tavanashad V, Passalacqua A, Fox RO, Subramaniam S. Effect of density ratio on velocity fluctuations in dispersed multiphase flow from particle-resolved numerical simulation. In: *71st Annual Meeting of the American Physical Societys Division of Fluid Dynamics*. Atlanta, GA, USA; 2018:.
63. Tomiyama A, Kataoka I, Zun I, Sakaguchi T. Drag coefficients of single bubbles under normal and micro gravity conditions. *JSME Int J Ser B* 1998;41(2):472–9. doi:10.1299/jsmeb.41.472.
64. Katz J, Meneveau C. Wake-induced relative motion of bubbles rising in line. *Int J Multiphase Flow* 1996;22(2):239–58. doi:10.1016/0301-9322(95)00081-X.
65. Zuber N. On the dispersed two-phase flow in the laminar flow regime. *Chem Eng Sci* 1964;19(11):897–917. doi:10.1016/0009-2509(64)85067-3.
66. Wijngaarden LV, Jeffrey DJ. Hydrodynamic interaction between gas bubbles in liquid. *J Fluid Mech* 1976;77(1):27–44. doi:10.1017/S0022112076001110.
67. Biesheuvel A, Spoelstra S. The added mass coefficient of a dispersion of spherical gas bubbles in liquid. *Int J Multiphase Flow* 1989;15(6):911–24. doi:10.1016/0301-9322(89)90020-7.
68. Béguin C, Pelletier É, Étienne S. Void fraction influence on added mass in a bubbly flow. *Eur J Mech B/Fluids* 2016;56:28–45. doi:10.1016/j.euromechflu.2015.11.008.
69. Spelt PD, Sangani AS. Properties and averaged equations for flows of bubbly liquids. *Appl Sci Res* 1997;58(1):337–86. doi:10.1023/A:1000856308915.

70. Simcik M, Ruzicka M. Added mass of dispersed particles by CFD: further results. *Chem Eng Sci* 2013;97:366–75. doi:10.1016/j.ces.2013.04.041.
71. Bridge AG, Lapidus L, Elgin JC. The mechanics of vertical gas–liquid fluidized system I: countercurrent flow. *AIChE J* 1964;10(6):819–26. doi:10.1002/aic.690100610.
72. Lockett M, Kirkpatrick R. Ideal bubbly flow and actual flow in bubble columns. *Trans Inst Chem Eng* 1975;53:267–73.
73. Rusche H, Issa R. The effect of voidage on the drag force on particles, droplets and bubbles in dispersed two-phase flow. In: *Japanese European Two-Phase Flow Meeting*. Tsukuba, Japan; 2000:.
74. Roghair I, Lau Y, Deen N, Slagter H, Baltussen M, Annaland MVS, Kuipers J. On the drag force of bubbles in bubble swarms at intermediate and high Reynolds numbers. *Chem Eng Sci* 2011;66(14):3204–11. doi:10.1016/j.ces.2011.02.030.
75. Roghair I, Van Sint Annaland M, Kuipers HJAM. Drag force and clustering in bubble swarms. *AIChE J* 2013;59(5):1791–800. doi:10.1002/aic.13949.
76. Simonnet M, Gentric C, Olmos E, Midoux N. Experimental determination of the drag coefficient in a swarm of bubbles. *Chem Eng Sci* 2007;62(3):858–66. doi:10.1016/j.ces.2006.10.012.
77. Gillissen JJJ, Sundaresan S, Van Den Akker HEA. A lattice Boltzmann study on the drag force in bubble swarms. *J Fluid Mech* 2011;679:101–21. doi:10.1017/jfm.2011.125.
78. Wray AA. Minimal storage time advancement schemes for spectral methods. NASA Ames Research Center; 1986.